Nanoscale

ROYAL SOCIETY OF CHEMISTRY

COMMUNICATION

View Article Online
View Journal | View Issue

Cite this: *Nanoscale*, 2020, **12**, 1414

Received 28th September 2019,
Accepted 19th December 2019

DOI: 10.1039/c9nr08352a

rsc.li/nanoscale

A unique pathway of PtNi nanoparticle formation observed with liquid cell transmission electron microscopy†

Liyun Zheng, *[a,b,c] Lixin Zhao,[b] Songhao Zhao,[b] Xiaowei Zhang,[d] Karen C. Bustillo,[e] Yuan Yao,[f] Xiaofei Yi,[g,h] Minggang Zhu,[a] Wei Li*[a] and Haimei Zheng *[c,i]

An understanding of nanoparticle growth is significant for controlled synthesis of nanomaterials with desired physical and chemical properties. Here we report the *in situ* study of platinum-nickel alloy nanoparticle growth using *in situ* liquid cell transmission electron microscopy (TEM). The observation revealed that Ni dendrites can form at the beginning and subsequently PtNi nanoparticles nucleate and grow by consumption of the Ni dendrites. The resulting PtNi alloy nanoparticles have a narrow size distribution with an average diameter of 3.7 nm, which are smaller than those obtained *via* classical solution growth. This work shed light on using such a unique growth pathway for the synthesis of novel nanoparticles.

Platinum based alloy nanostructures, Pt–M (M = Co, Ni, Fe, *etc.*), have attracted attention in recent years due to their potential use in biosensor devices,[1] fuel cells,[2] solar cells,[3] magnetic data storage devices,[4,5] and in the field of catalysis.[6,7] Platinum based nanoparticles often have novel optical, electronic, magnetic and catalytic properties that are related to their size, shape and structure.[8–10] Understanding nanocrystal formation is essential for controlled synthesis of nanocrystals with the desired morphology and structure dependent physical and chemical properties.

Nanoparticles with varying size and morphology have been synthesized in solution.[11,12] Several models have been developed to understand nanoparticle growth, such as LaMer model,[13,14] Ostwald ripening,[15] Finke–Watzky mechanism,[16] coalescence[17] and orientated attachment,[18] and intraparticle growth.[19,20] In this paper, we report a unique pathway of PtNi nanoparticle formation that has not been observed previously and cannot be explained by these models to the best of our knowledge.

In situ liquid cell transmission electron microscopy (TEM) has been used to directly observe nanoparticle growth trajectories in liquids in real time with high spatial resolution.[20,21] The technique can provide key information about nanoparticle formation mechanisms. Besides imaging of nanoparticle growth,[22,23] liquid cell TEM has been used to study nanoparticle self-assembly,[24] electrochemical deposition,[25] and biological materials in liquid water.[26] In our previous work,[27] we obtained core–shell PtNi–Ni nanoparticles by liquid cell TEM. Here, we use liquid cell TEM to further study Pt–Ni alloy nanoparticles using a higher solute concentration, of interest because of their excellent catalytic properties.

All chemicals were used as-received from Sigma-Aldrich Co., including Pt(acetylacetonate)$_2$ (99%, Pt(acac)$_2$), Ni(acetylacetonate)$_2$ (99%, Ni(acac)$_2$), oleylamine(98%), oleic acid (99%), and benzyl ether (99%). The growth solution used was 0.3 mmol of Pt(acac)$_2$ and Ni(acac)$_2$ in total as precursors and the ratio of Pt : Ni was 1 : 1. We prepared the growth solution by dissolving Pt(acac)$_2$, Ni(acac)$_2$ in 0.3 ml benzyl ether in the presence of 5.4 ml oleylamine and 0.6 ml, 0.3 ml, 0.1 ml oleic acid (total 6.3 ml, 6 ml, 5.8 ml solution). The chemicals were heated to 50 °C under magnetic stirring for 1 hour in order to obtain a homogenous mixture. Heating slightly above room temperature facilitates dissolution but no particle growth is initiated. This uniform solution was used for liquid cell loading.

About 100 nanoliters of growth solution was loaded into a liquid cell by capillary force forming a thin liquid layer sand-

[a]*Division of Functional Materials, Central Iron and Steel Research Institute, Beijing, 100081, China. E-mail: zhengliyun@126.com, weili@cisri.com.cn*
[b]*College of Materials Science and Engineering, Hebei University of Engineering, Handan, Hebei 056011, China*
[c]*Materials Sciences Division, Lawrence Berkeley National Laboratory, Berkeley, California 94720, USA. E-mail: hmzheng@lbl.gov*
[d]*Department of Electrical Engineering and Computer Science, Ningbo University, Ningbo, Zhejiang 315211, China*
[e]*National Center for Electron Microscopy, Molecular Foundry, Lawrence Berkeley National Laboratory, Berkeley, California 94720, USA*
[f]*Institute of Physics, Chinese Academy of Science, Beijing 100190, China*
[g]*State Key Laboratory of Rare Earth Permanent Magnetic Materials, Hefei, Anhui 340124, China*
[h]*Earth-Panda Advance Magnetic Materials Co., Ltd, Hefei, Anhui 340124, China*
[i]*Department of Materials Science and Engineering, University of California, Berkeley, California 94720, USA*

†Electronic supplementary information (ESI) available. See DOI: 10.1039/c9nr08352a

wiched between two silicon nitride membranes.[17] The *in situ* TEM studies were performed using a JEOL 3010 TEM with a LaB_6 cathode operating at 300 kV. Nucleation and growth was initiated by the electron beam and the electron beam dose rate in the range of 2000–4500 $e^- Å^{-2} s^{-1}$. Inside each liquid cell several movies were recorded in different locations. Complimentary *ex situ* TEM studies were performed using a FEI F20 Tecnai instrument equipped with a Gatan image filter operating at 200 kV, a FEI 80–300 Titan operating at 200 kV with a Bruker Quantax energy-dispersive X-ray spectrometry (EDS) detector and a JEOL ARM200F Cs Corrected S/TEM with electron energy loss spectrometer (EELS). Detailed descriptions of liquid cell preparation and imaging conditions can be found in the ESI.†

When $Pt(acac)_2$ and $Ni(acac)_2$ dissolved in 0.3 ml benzyl ether in the presence of 5.4 ml oleylamine and 0.6 ml oleic acid (total 6.3 ml solution), the solute concentration was 0.045 M, we obtained PtNi nanoparticles directly (see ESI Movie S1†). When $Pt(acac)_2$ and $Ni(acac)_2$ dissolved in 0.3 ml benzyl ether in the presence of 5.4 ml oleylamine and 0.3 ml oleic acid, the solute concentration was 0.05 M, we observed a two-stage growth of PtNi nanoparticles, including the initial formation of Ni dendrites and the subsequent growth of PtNi alloy nanoparticles. When $Pt(acac)_2$ and $Ni(acac)_2$ dissolved in 0.3 ml benzyl ether in the presence of 5.4 ml oleylamine and 0.1 ml oleic acid and the solute concentration was 0.052 M, we also obtained the similar two-stage growth of PtNi nanoparticles. So, the critical concentration for the two-stage growth should be a range between 0.045 M and 0.05 M. All the above experiments performed under an electron beam dose rate of 3510 $e^- Å^{-2} s^{-1}$. We have changed the electron beam dose rate in the range of 2000–4500 $e^- Å^{-2} s^{-1}$ and found that the dendrite and followed nanoparticles growth speed increased with the increase of electron beam dose rate, which has less effect on the morphologies of dendrite and the followed nanoparticles.

The two-step growth behaviour and the growth kinetics are shown in Fig. 1 (also see ESI Movie S2†). Sequential images show the development of Ni dendrites from nanoparticles during the early stage followed by the formation of many PtNi nanoparticles in the central regions of the dendrites. The area of the Ni dendrite changes with time and is plotted in Fig. 1B, which shows that dendrites grow quickly and their area increases to approximately 9710 nm^2 in 40 seconds. The number of PtNi nanoparticles and the particle size evolution are plotted as a function of time in Fig. 1C with black and blue lines, respectively. Most nanoparticles grow by atomic attachment forming spheres, while some nanoparticles coalesce with one or more neighbor particles experiencing shape changes. All PtNi nanoparticles are of spherical shape eventually. The growth of PtNi nanoparticles proceeds by consuming the Ni dendrites gradually. In the end, only the outer parts of the Ni dendrite remain.

The kinetics of particle growth follows $R/R_0 \sim t^{\beta}$, where R is the radius of nanoparticle, R_0 is the critical radius of nuclei of nanoparticle, and β is the growth exponent.[28] The average

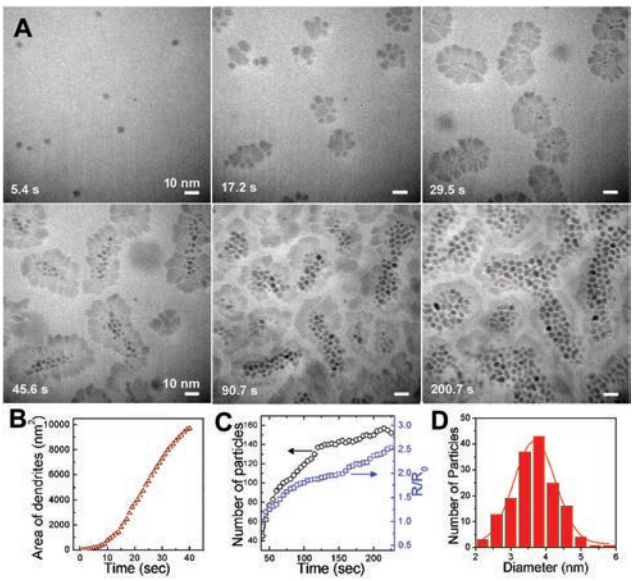

Fig. 1 Growth trajectory during the two-stage dendritic pathway resulting in PtNi nanoparticles. (A) Sequential images captured during the growth process; (B) area of dendrite *versus* time; (C) plot of particle numbers (black dot) and particle size evolution (blue square) as a function of time; (D) size distribution of nanoparticles.

growth exponent of the nanoparticles, β, is calculated to be 0.14 (Fig. 1C blue), falling in the region of diffusion-limited growth of the Lifshitz–Slyozoy–Wagner model.[28] This type of growth is consistent with other reports on nanoparticle growth in a TEM liquid cell.[29,30] Fig. 1D shows the particle size distribution, where an average diameter of 3.7 nm is obtained.

Fig. 2 shows that at the initial stage dendritic nanostructures are formed (also see ESI Movie S2†). The selected area electron diffraction (SAED) pattern of the dendrites (in Fig. 2A) best matches with the Joint Committee on Powder Diffraction Standards (JCPDS) card 45-1027 (also see ESI Fig. S1 and Table S1†), a hexagonal Ni structure.[31] We further performed electron energy loss spectroscopy (EELS), which shows the Ni L-edge from a dendrite is consistent with that of the Ni L_3–L_2 edge (Fig. 2C).[32]

Fig. 3 shows the X-ray energy dispersive spectroscopy (EDS) maps of the dendrites and the initial formation of PtNi nanoparticles at the center and corners of the Ni dendrites. In the

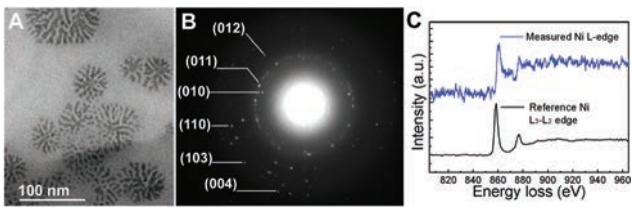

Fig. 2 Ni dendrite (A) TEM; (B) SAED of dendrite region; (C) measured EELS spectrum from dendrite showing the Ni L-edge of dendrite in (A) synthesized in the initial stage (blue) and a reference Ni L3–L2 edge (black, bottom spectrum, ref. 32).

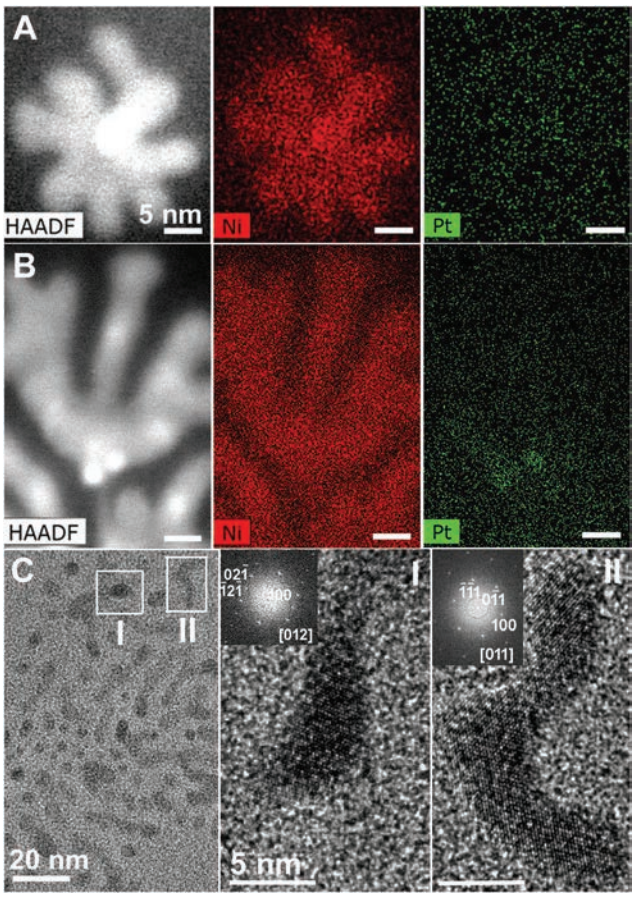

Fig. 3 STEM-HAADF image and elemental EDS maps for (A) a small dendrite, (B) part of a large dendrite with Pt–Ni nanoparticle. (C) TEM image and HRTEM of the remaining Ni dendrite of white squares (I and II, in set FFT image) in the second stage under the electron beam irradiation of the precursor solution.

initial stage, the dendrite formed (shown in Fig. 3A). Ni is distributed throughout the entire dendrite, while Pt can be found in the central regions corresponding to the bright contrast observed in the high angle annular dark field (HAADF) image (Fig. 3B). From the high-resolution TEM (HRTEM) images and the inset fast Fourier transform (FFT) images (Fig. 3C), the dendrites are observed to have a hexagonal structure (see ESI Fig. S2 and S3†). Fig. 3C shows that the Ni hexagonal structure still existed at the outer edge of dendrite simultaneously during the transformation of Ni to PtNi.

Further EDS mapping of the nanoparticles converted from dendrites shows the presence of both Pt and Ni (Fig. 4A). In the residue dendrite, only Ni was detected with a diffraction pattern that is consistent with the Ni hexagonal structure. By fitting the Pt L-edge peak and the Ni K-edge peak of the PtNi nanoparticles, we quantify the composition using Cliff-Lorimer factors to account for the scattering cross-sections of the X-ray peaks.[33] The results show that the Pt : Ni ratio is approximately 1 : 1 (see ESI Table S2†). HRTEM images of a large number of nanoparticles (Fig. 4B as examples) show PtNi nanoparticles have monocrystalline structure and an interplanar spacing of 0.2193 nm, which matches the (111) facet of cubic PtNi (JCPDS card (65-9445).[34]

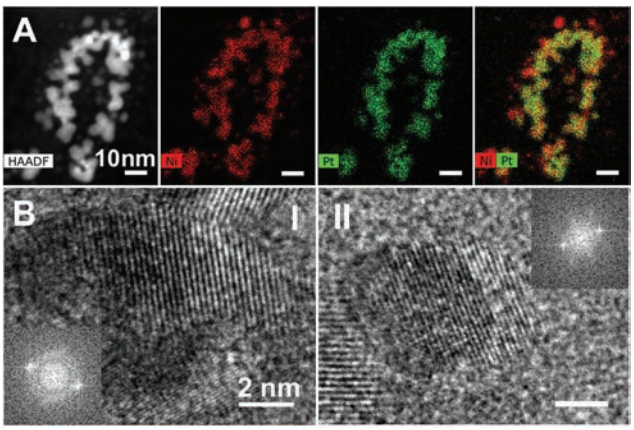

Fig. 4 Fully formed PtNi nanoparticles. (A) HAADF image and EDS elemental maps of Ni, Pt and composite of Ni and Pt, (B) HRTEM for the nanoparticles formed in the center of the dendrite from Fig. 3(A), B I shows the facet (111) for cubic PtNi and B II shows the facet (200) for cubic PtNi.

In Fig. 5, the cartoon images highlight the sequential reactions and PtNi nanoparticle growth pathway. In the beginning Ni dendrites formed (steps I and II). Subsequently, PtNi nanoparticles were formed by consuming Ni dendrites (step III). The nucleation of PtNi was initiated by the reduction of Pt^{2+} to Pt^0. Oleylamine ligands ($R\text{-}NH_2$) prefer to bond to Pt which catalyzes the electron transfer between oleylamine and the metal ions,[35] and Ni can be converted to PtNi. PtNi nanoparticles are found at the central regions of the Ni dendrites, especially at the edges or angular parts, which is likely due to the higher energy at the edge of dendrites with a high concentration of grain boundaries.

The observed synthesis pathway for PtNi nanoparticles is clearly different than the classical nucleation and growth of colloidal nanoparticles from solution, where nuclei that are larger than a critical size grow to form nanoparticles.[27,35–37] In our previously studied PtNi–Ni growth in a liquid cell,[27] nucleation and growth of core–shell PtNi–Ni nanoparticles was observed in the PtNi system as described by the following steps. First Pt clusters' nucleation is initiated by focusing the electron beam. The Pt^{2+} ions are reduced to platinum metal by the assistance of oleylamine or by the solvated free-electrons from inelastic scattering of the incident electron beam.[27] And then Ni^{2+} ions are reduced with Pt atom catalyzation and oleylamine reduction and formed PtNi alloy nanoparticles. When the Pt is depleted in the precur-

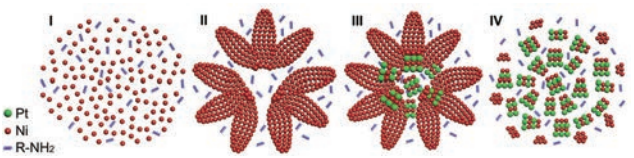

Fig. 5 Schematic illustration of the growth pathway of PtNi nanoparticles from Ni dendrites.

sor solution, the core size is defined and then the Ni sheath forms. In contrast to the core–shell PtNi–Ni pathway, the Pt–Ni nanoparticle pathway in this work starts with an initial deposition of Ni in the form of dendrites. This is probably because of the higher solute concentration and phase spinodal in the precursor solution.[38,39] The precursor solution heated to 50 °C under magnetic stirring for 1 hour in this work was uniform initially and has a far higher concentration than the room-temperature saturation concentration of $Ni(acac)_2$ and $Pt(acac)_2$ in the solvent of benzyl ether, oleic acid and oleylamine. Thus, it is reasonable that nickel-platinum binary system is within its spinodal region.[38] As described in ref. 38, the solution with much higher supersaturations near the spinodal lost all resemblance to a classical nucleus. For example, the free energy approaches zero and no part of the nucleus is even approximately homogeneous. Under the electron beam irradiation, the supersaturated solution demixed into nickel-rich and nickel-poor phase by spinodal decomposition. The nickel ions in the nickel-rich area got electrons and formed atoms. And then nickel atoms nucleated, grew rapidly and formed anisotropic dendrites, which is consistent with the observed fast growth of Ni dendrites.

We have ever changed the electron beam dose rate in the range of 2000–4500 e^{-} $Å^{-2}$ s^{-1} and found that the dendrite and followed nanoparticles growth speed increased with the increase of electron beam dose rate. The electron beam dose rate in this work has less effect on the morphologies of dendrites and the followed nanoparticles.

In conclusion, we observed a novel two-stage growth mechanism of Pt–Ni binary alloy nanostructures. PtNi nanoparticles can be synthesized using colloidal chemistry and electron beam initiation in the TEM. The growth pathway follows dendritic growth of Ni followed by precipitation of PtNi binary alloy nanoparticles in the center of the Ni dendrites.

Conflicts of interest

There are no conflicts to declare.

Acknowledgements

We used JEOL 3010, FEI Tecnai and FEI Titan microscopes for *in situ* and *ex situ* analysis at the National Center for Electron Microscopy, Molecular Foundry of the Lawrence Berkeley National Laboratory (LBNL) under the proposal of No. 3818. L. Z. acknowledges the support of China Scholarship Council (CSC) under No. 201408130046, the Key R & D Program Projects of Hebei under No. 19211008D and the Natural Science Foundation of Hebei of China under No. E2017402039 and No. E2017402139.

Notes and references

1 X. Zhu, X. Niu, H. Zhao, J. Tang and M. Lan, *Biosens. Bioelectron.*, 2015, **67**, 79.
2 P. Mani, R. Srivastava and P. Strasser, *J. Phys. Chem. C*, 2008, **112**, 2770.
3 Y. Xiao, G. Han, Y. Li, M. Li and J.-Y. Lin, *J. Power Sources*, 2015, **278**, 149.
4 H. Zeng, S. Sun, J. Li, Z. L. Wang and J. P. Liu, *Appl. Phys. Lett.*, 2004, **85**, 792.
5 H. Zeng, J. Li, Z. L. Wang, J. P. Liu and S. Sun, *Nano Lett.*, 2004, **4**, 187.
6 W. Yu, M. D. Porosoff and J. G. Chen, *Chem. Rev.*, 2012, **112**, 5780.
7 B. Y. Xia, H. B. Wu, N. Li, Y. Yan, X. W. Low and X. Wang, *Angew. Chem.*, 2015, **127**, 3868.
8 L. Chen, J. M. Chabu and Y. Liu, *RSC Adv.*, 2013, **3**, 4391.
9 R. K. Leary, A. Kumar, P. J. Straney, S. M. Collins, S. Yazdi, R. E. Dunin-Borkowski, P. A. Midgley, J. E. Millstone and E. Ringe, *J. Phys. Chem. C*, 2016, **120**, 20843.
10 A. T. N. Dao, D. M. Mott, K. Higashimine and S. Maenosono, *Sensors*, 2013, **13**, 7813.
11 J.-J. Du, Y. Yang, R.-H. Zhang and X.-W. Zhou, *Mater. Chem. Phys.*, 2015, **155**, 47.
12 V. R. Stamenc, B. S. Mun, M. Arenz, K. J. J. Mayrhofer, C. A. Lucas, G. Wang, P. N. Ross and N. M. Markovic, *Nat. Mater.*, 2007, **6**, 241.
13 V. K. LaMer and R. H. Dinegar, *J. Am. Chem. Soc.*, 1950, **72**, 4847.
14 V. K. LaMer, *Ind. Eng. Chem.*, 1952, **44**, 1270.
15 M. Di Vece, D. Grandjean, M. J. Van Bael, C. P. Romero, X. Wang, S. Decoster, A. Vantomme and P. Lievens, *Phys. Rev. Lett.*, 2008, **100**, 236105.
16 M. A. Watzky and R. G. Finke, *Chem. Mater.*, 1997, **9**, 3083.
17 H. Zheng, R. K. Smith, Y. W. Jun, C. Kisielowski, U. Dahmen and A. P. Alivisatos, *Science*, 2009, **324**, 1309.
18 D. Li, M. H. Nielsen, J. R. I. Lee, C. Frandsen, J. F. Banfield and J. J. De Yoreo, *Science*, 2012, **336**, 1014.
19 X. Peng, L. Manna, W. Yang, J. Wickham, E. Scher, A. Kadavanich and A. P. Alivisatos, *Nature*, 2000, **404**, 59.
20 Z. A. Peng and X. Peng, *J. Am. Chem. Soc.*, 2001, **123**, 1389.
21 H. G. Liao and H. Zheng, *Annu. Rev. Phys. Chem.*, 2016, **67**, 719.
22 H.-G. Liao, D. Zherebetskyy, H. Xin, C. Czarnik, P. Ercius, H. Elmlund, M. Pan, L. W. Wang and H. Zheng, *Science*, 2014, **345**, 916.
23 E. Sutter, K. Jungjohann, S. Bliznakov, A. Courty, E. Maisonhaute and P. Sutter, *Nat. Commun.*, 2014, **5**, 4946.
24 H.-G. Liao, L. Cui, S. Whitelam and H. Zheng, *Science*, 2012, **336**, 1011.
25 Z. Zeng, W.-I. Liang, H.-G. Liao, H. L. Xin, Y. H. Chu and H. Zheng, *Nano Lett.*, 2014, **14**, 1745.
26 U. Mirsaidov, H. Zheng, Y. Casana and P. Matsudaira, *Biophys. J.*, 2012, **102**, L15.
27 L. Zheng, X. Zhang, K. C. Bustillo, Y. Yao, L. Zhao, M. Zhu, W. Li and H. Zheng, *Nanoscale*, 2018, **10**, 11281.
28 I. M. Lifshitz and V. V. Slyozov, *J. Phys. Chem. Solids*, 1961, **19**, 35.
29 Y. Liu, K. Tai and S. Dillon, *Chem. Mater.*, 2013, **25**, 2927–2933.

30 D. Bhattacharya, M. Bosman, V. R. S. S. Mokkapati, F. Y. Leong and U. Mirsaidov, *Microsc. Microanal.*, 2014, **20**, 407.
31 C. N. Chinnasamy, B. Jeyadevan, K. Shinoda, K. Tohji, A. Narayanasamy, K. Sato and S. Hisano, *J. Appl. Phys.*, 2005, **97**, 10J309.
32 E. C. Dickey, X. Fan and S. J. Pennycook, *Acta Mater.*, 1999, **47**, 4061.
33 R. J. Graham and J. W. Steeds, *J. Microsc.*, 1984, **133**, 275.
34 S. C. Zignani, V. Baglio, D. Sebastián, A. Saccà, I. Gatto and A. S. Aricò, *Materials*, 2017, **10**, 317.
35 W.-I. Liang, X. Zhang, Y. Zan, M. Pan, C. Czarnik, K. Bustillo, J. Xu, Y. Chu and H. Zheng, *J. Am. Chem. Soc.*, 2015, **137**, 14850.
36 W. B. Russell, *Phase Transitions*, 1990, **21**, 127.
37 T. Kawasaki and H. Tanaka, *Proc. Natl. Acad. Sci. U. S. A.*, 2010, **107**, 14036.
38 J. W. Cahn and J. E. Hilliard, *J. Chem. Phys.*, 1959, **31**, 688.
39 N. D. Loh, S. Sen, M. Bosman, S. F. Tan, J. Zhong, C. A. Nijhuis, P. Kral, P. Matsudaira and U. Mirsaidov, *Nat. Chem.*, 2016, **1**, 77.